Solar Physics
DOI: 10.1007/•••••-•••-•••-••••-•

A Challenging Solar Eruptive Event of 18 November 2003 and the Causes of the 20 November Geomagnetic Superstorm. III. Catastrophe of the Eruptive Filament at a Magnetic Null Point and Formation of an Opposite-Handedness CME

A.M. Uralov[1] · **V.V. Grechnev**[1] · **G.V. Rudenko**[1] · **I.I. Myshyakov**[1] · **I.M. Chertok**[2] · **B.P. Filippov**[2] · **V.A. Slemzin**[3]

Received ; accepted

© Springer ••••

Abstract Our analysis in Papers I and II (Grechnev *et al.*, 2014, Solar Phys. 289, 289 and 1279) of the 18 November 2003 solar event responsible for the 20 November geomagnetic superstorm has revealed a complex chain of eruptions. In particular, the eruptive filament encountered a topological discontinuity located near the solar disk center at a height of about 100 Mm, bifurcated, and transformed into a large cloud, which did not leave the Sun. Concurrently, an additional CME presumably erupted close to the bifurcation region. The conjectures about the responsibility of this compact CME for the superstorm and its disconnection from the Sun are confirmed in Paper IV (Grechnev *et al.*, Solar Phys., submitted), which concludes about its probable spheromak-like structure. The present paper confirms the presence of a magnetic null point near the bifurcation region and addresses the origin of the magnetic helicity of the interplanetary magnetic clouds and their connection to the Sun. We find that the orientation of a magnetic dipole constituted by dimmed regions with the opposite magnetic polarities away from the parent active region corresponded to the direction of the axial field in the magnetic cloud, while the pre-eruptive filament mismatched it. To combine all of the listed findings, we come to an intrinsically three-dimensional scheme, in which a spheromak-like eruption originates *via* the interaction of the initially unconnected magnetic fluxes of the eruptive filament and pre-existing ones in the corona. Through a

[1] Institute of Solar-Terrestrial Physics SB RAS, Lermontov St. 126A, Irkutsk 664033, Russia email: uralov@iszf.irk.ru
[2] Pushkov Institute of Terrestrial Magnetism, Ionosphere and Radio Wave Propagation (IZMIRAN), Moscow, Troitsk, 142190 Russia email: ichertok@izmiran.ru, bfilip@izmiran.ru
[3] P.N. Lebedev Physical Institute, Leninsky Pr., 53, Moscow, 119991, Russia email: slem@lebedev.ru

arXiv:1404.3515v2 [astro-ph.SR] 26 May 2014

chain of magnetic reconnections their positive mutual helicity was transformed into the self-helicity of the spheromak-like magnetic cloud.

Keywords: Active Regions, Solar Eruptions, Coronal Magnetic Null, Magnetic Clouds, Helicity, Implications of Reconnection

1. Introduction

An extreme geomagnetic storm on 20 November 2003 was caused by the interaction of the Earth's magnetosphere with an interplanetary magnetic cloud (MC), whose magnetic helicity, $H_{\rm m}$, was positive. The very strong magnetic field in the MC of up to $|B|_{\max} \approx 56$ nT had a long-lasting negative B_z component (up to $B_{z\,\max} \approx -46$ nT). These circumstances were crucial in identifying the solar source for the MC. Gopalswamy *et al.* (2005) and Yurchyshyn, Hu, and Abramenko (2005) definitely associated the MC with the filament eruption in the active region (AR) 10501 (we will use henceforth the last three digits for brevity) on 18 November. These authors considered the direction of the axial magnetic field in the pre-eruptive filament to correspond to the expected projection $B_z < 0$. With such a direction of the axial field, the current helicity of the filament, $H_{\rm c}$, is positive. From the condition $\mathrm{sign}(H_{\rm m}) = \mathrm{sign}(H_{\rm c})$, which is valid for a linear force-free magnetic field, it follows that the magnetic helicity is also positive. Later Möstl *et al.* (2008) found a correspondence between the flare reconnected magnetic flux, measured as the flare ribbon flux, and the poloidal magnetic flux of the MC under the assumption that the MC was a part of a magnetic flux rope with a length of 0.5–2 AU. The studies by Gopalswamy *et al.* (2005), Yurchyshyn, Hu, and Abramenko (2005), and Srivastava *et al.* (2009) gave the impression of an acceptable correspondence between the conditions of the eruption in AR 501 and the parameters of the MC observed in the Earth orbit: $H_{\rm m} > 0, B_z < 0$.

The study of Chandra *et al.* (2010) changed this situation. From the observed morphological features they found that the large-scale magnetic field in AR 501 had a negative helicity sign. This finding seemingly contradicted what was expected from the magnetic helicity conservation requiring the same sign of the magnetic helicity in the AR and MC. This circumstance has raised a question, why the AR, which had a global negative magnetic helicity, could expel a positive-helicity MC to the interplanetary medium.

One possible answer was proposed by Chandra *et al.* (2010), who found a localized positive helicity injection in the southern part of AR 501 and concluded that the right handedness of the observed MC was due to the ejection from this portion of the AR. On the other hand, Leamon *et al.* (2004) in their study of 12 interplanetary MCs and related solar active regions have found: *i*) a significant difference between the total twist of the magnetic field inside active regions, $(\alpha L)_{\rm AR}$, and that in the MC, $(\alpha L)_{\rm MC}$; *ii*) the absence of any significant sign relationship between them. The authors used the linear force-free approximation, α is a constant. The dipole scale, $L_{\rm AR}$, was measured as the distance between the centroids of the positive and negative fluxes in the

magnetogram of an AR. The magnetic field in an MC was fit with the Lundquist magnetic model with $L_{\rm MC} = 2.5$ AU length. Findings (*i*) and (*ii*) have compelled Leamon *et al.* (2004) to conclude that "*magnetic clouds associated with active region eruptions are formed by magnetic reconnection between these regions and their larger-scale surroundings, rather than simple eruption of preexisting structures in the corona or chromosphere*". Zhang and Low (2003) described a similar phenomenon analytically by using the idealized example of the axially-symmetric reconfiguration of two twisted magnetic fluxes from their unconnected initial state to the connected relaxed state. They have shown that magnetic reconnection can reverse the twist direction of a flux rope emerging into preexisting fields under the conservation of the total relative magnetic helicity. The complex reconnection of a flux rope with the adjacent field in complex magnetic topology has been also described by, *e.g.*, Lugaz *et al.* (2011), Zuccarello *et al.* (2012), and Masson, Antiochos, and DeVore (2013).

Grechnev *et al.* (2008, 2011a, 2013) have found observational evidence of magnetic reconnection between the internal field belonging to the eruptive filament and the preexisting coronal field. This is a phenomenon of plasma dispersal from an eruptive filament over the solar surface that is visible as the disintegration of the filament. The whole mass of an eruptive filament or a considerable fraction of its mass does not leave the Sun as a part of a CME. The motion of the cool plasma of the eruptive filament continues along new magnetic field lines passing inside the eruptive filament and ending far on the solar surface. Clouds of such plasma can screen the emission of compact sources in active regions as well as the emission from quiet solar areas. Absorption phenomena can be observed in microwaves and also in the He II 304 Å line. Events of such a kind are associated with active region eruptions. They have been rarely detected for observational reasons.

The analysis of the solar geoeffective event of 18 November 2003 by Grechnev *et al.* (2014c) (hereafter Paper I) and Grechnev *et al.* (2014b) (hereafter Paper II) has revealed that the major eruption in this event, *i.e.*, the eruption of the U-shaped filament, which we call F1, from AR 501, was also not a simple one. The eruptive filament bifurcated and transformed into a large Y-shaped cloud, which moved from the region of bifurcation (Rb) to the South–West across the solar disk toward the limb. Figure 1 illustrates what has happened to the eruptive filament, as shown by the Hα images produced by the Kanzelhöhe Solar Observatory (KSO), the *Extreme-ultraviolet Imaging Telescope* (EIT; Delaboudinière *et al.*, 1995), on board the *Solar and Heliospheric Observatory* (SOHO), and the *Spectroheliographic X-ray Imaging Telescope* (SPIRIT; Zhitnik *et al.* (2002) and Slemzin *et al.* (2005)), on board the *Complex Orbital near-Earth Observations of Activity of the Sun* (CORONAS-F) satellite (Oraevsky and Sobelman, 2002; Oraevsky *et al.*, 2003).

The masses of the Y-like cloud and the pre-eruption filament were similar (Paper I); on the other hand, remnants of the filament were not evident in the southwestern CME observed by the *Large Angle and Spectrometric Coronagraph* (LASCO) that was previously regarded as the source of the 20 November geomagnetic storm. The observations analyzed in Paper I and Paper II suggest a possible additional eruption in the interval from 08:07 to 08:14 UT above the bifurcation region close to the solar disk center that could be the source of the

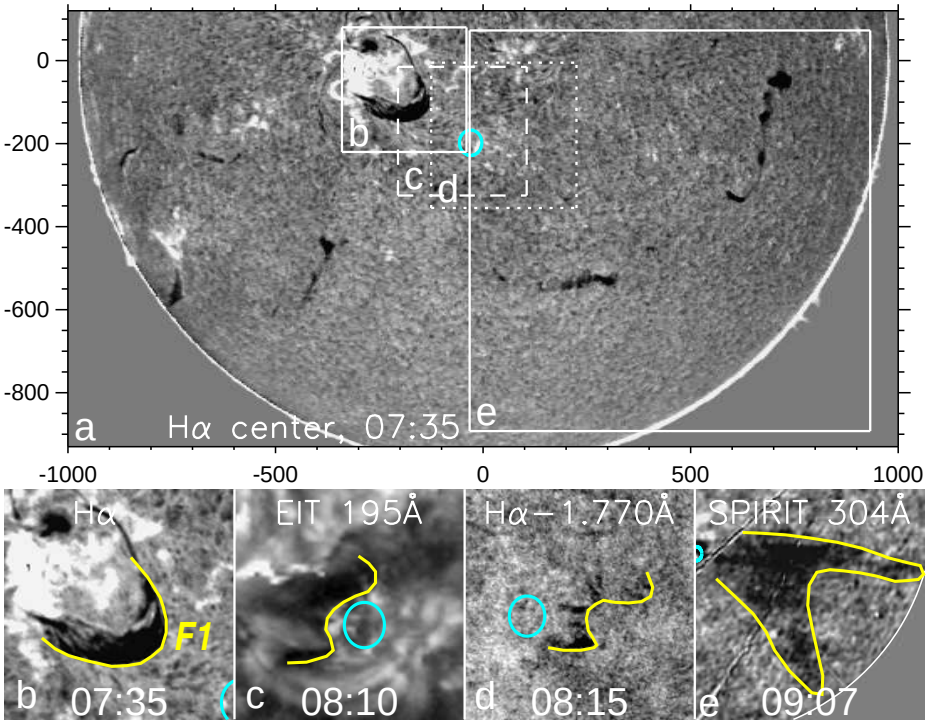

Figure 1. Bifurcation of the main eruptive filament F1. (a,b) Pre-eruption Hα line-center image (KSO). The frames denote the fields of view of the four images shown in the lower row (b–e). The axes are in arc seconds from the solar disk center. The turquoise oval in all the images denotes the region Rb where the filament bifurcated. The yellow curves roughly outline the frontal edge of the filament before and during the eruption. (c) SOHO/EIT image in the 195 Å channel. (d) KSO Hα image observed in the far blue wing. (e) Y-like cloud in the CORONAS-F/SPIRIT 304 Å image.

interplanetary MC on 20 November. These facts disfavor the simple scenario, in which the 20 November MC is considered as a flux rope formed directly from a structure initially associated with the pre-eruptive filament F1 in region 501.

As mentioned, the right-handed MC produced in this event and responsible for the superstorm had a very strong magnetic field near Earth of up to $|B|_{\max} \approx$ 56 nT and $B_{z\ \max} \approx -46$ nT. According to Möstl *et al.* (2008), its inclination to the ecliptic plane was $\theta = -(49-87)^\circ$, and the magnetic flux in this plane was 0.55×10^{21} Mx; however, its significant part could be lost by reconnection in the interplanetary space. In Grechnev *et al.* (2014a) (hereafter Paper IV), we additionally find that the MC was compact, with a size of about 0.2 AU, and had some atypical properties, such as a wide range of proton temperatures, from 2×10^4 K to 3×10^5 K; its magnetic structure was closed, disconnected from the Sun, and probably had a spheromak configuration.

The present paper (hereafter Paper III) endeavors to understand how the catastrophe of the eruptive filament could occur and create the right-handed spheromak-like MC. Section 2 outlines the eruptive event and results of its analysis. Section 3 analyzes the helicity in AR 501. In Section 4 we address

the causes of the bifurcation of the eruptive filament. In Section 5 we try to understand how the MC could be formed. Section 6 briefly summarizes the outcome of this study.

2. Outline of the Event and Observational Indications

2.1. Observational Results and Suggestions

Paper I and Paper II have revealed a few eruptive episodes in the complex event of 18 November 2003. Here we outline and illustrate them using the images from EIT in Figures 2a–2f and the time profiles in Figure 2g produced in hard X-rays (HXR) by the *Reuven Ramaty High-Energy Solar Spectroscopic Imager* (RHESSI: Lin *et al.*, 2002) and, for the RHESSI nighttime, in microwaves by the US Air Force *Radio Solar Telescope Network* radiometers in San Vito.

The pre-eruptive U-shaped filament F1 rooted in AR 501 was pointing in the plane of the sky toward a small ring-like structure Rb (Figure 2a). Active region 503 was located North of Rb. Episode E1 presumably gave rise to a first southeastern CME (CME1) responsible for am elongated dimming D1, which started to develop during the interval shown in Figure 2b. A jet-like ejection, Ej, in Figure 2c (E2) triggered the motion of filament F1, but did not produce any CME directly. The filament accelerated in a weak episode E3 (Figure 2g). The eruptive filament, whose trajectory crossed a topological discontinuity located at a height of about 100 Mm, collided with a coronal structure above Rb (E4A) and bifurcated (E4B), apparently rolling around it. In response to the interaction, brightenings overlapping Rb appeared in Figure 2d. They rotated clockwise and, after E4B, vanished in Figure 2e. Episode E4C was presumably related to the onset of the second southwestern CME (CME2). In Figure 2e, dimmings developed at the previous position of Rb and West of it (D2); a central brightening (not mentioned in Papers I and II) appeared in AR 503 (E4D), indicating its involvement in an eruption. After the chain of eruptions E1–E4, regions D1, D2, D3, and the former Rb region dimmed (Figure 2f); the bifurcated filament F1 apparently transformed into a Y-like 'cloud' moving across the solar disk (Figures 1c–1e).

One more ejection probably occurred near the solar disk center during the E4 burst (Figures 2d, 2e). The ejection was detected in Paper II as a faintly visible round feature, which expanded approximately from the position of the bifurcation region in the images produced by the *Solar X-ray Imager* (SXI) on board the *Geostationary Operational Environmental Satellite* (GOES-12). The observed radial expansion was coordinated with the trajectory of a drifting type IV radio burst in the dynamic radio spectrum using the acceleration profile in Figure 2h. The final speed of this radial expansion was $V_r \approx 100$ km s^{-1}. The mass of this ejection should be $\ll 5 \times 10^{15}$ g (see Paper I). The properties of the presumable ejection are very different from those of CME2 ejected at the same time, but appear to match the expectations for a source of the 20 November superstorm. This low-mass, weakly expanding ejection presumably moved along the Sun–Earth line, and therefore its meager Thomson-scattered

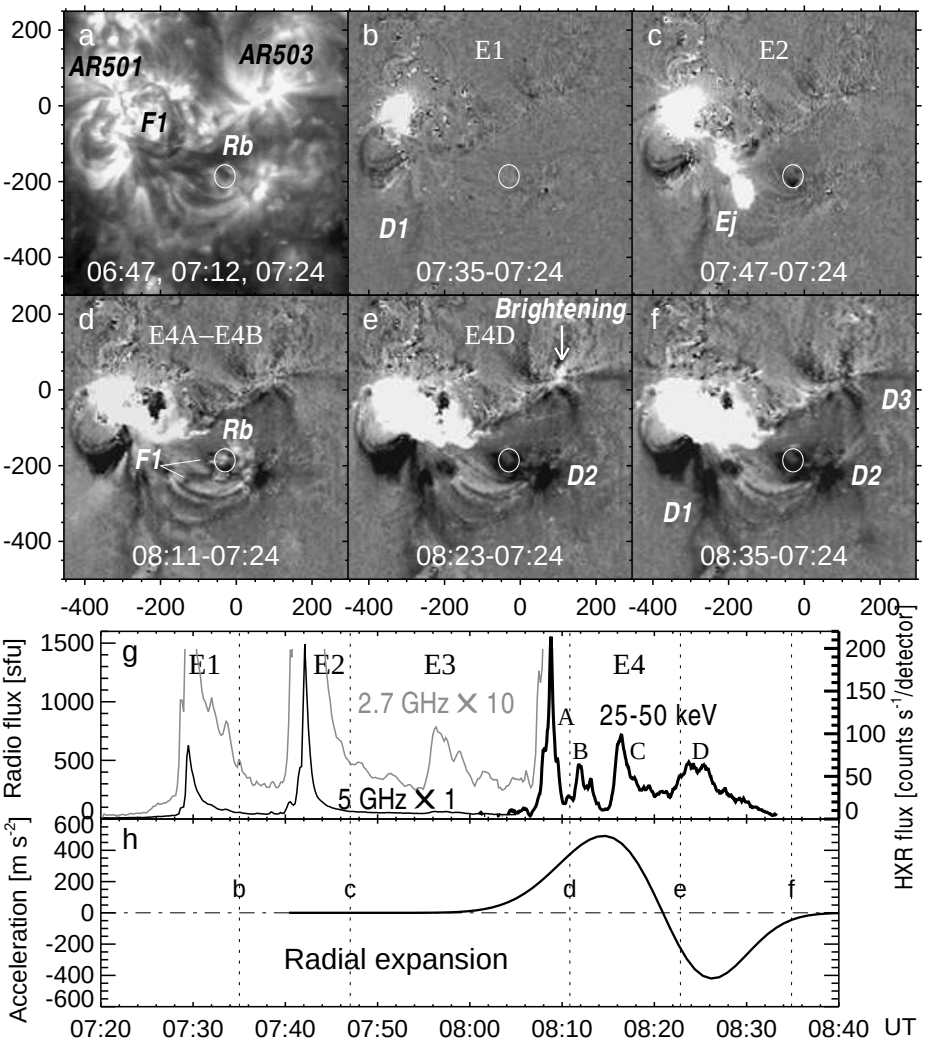

Figure 2. History of the event. (a) Pre-event situation in an averaged EIT 195 Å image, which is built with images taken at the hours indicated at the bottom of the panel. (b–f) Milestones in the event in the EIT 195 Å fixed-base difference images (the differences are taken between the hours indicated at the bottom of each panel). The solar rotation was compensated to 08:20 UT. The axes are in arc seconds from the solar disk center. (g) Time profiles in microwaves at 5 GHz (thin black line), 2.7 GHz (gray line, magnified by a factor of 10), and in HXR (thick black line). (h) The acceleration of the radial expansion of the invisible CME, which presumably erupted near the solar disk center close to region Rb. The labels E1–E4D in panels (b–f) denote the eruptive episodes marked in the time profiles in panel (g). The vertical dotted lines in panels (g) and (h) mark the observation times of panels (b–f).

light was insufficient to be detected by the LASCO coronagraphs. On the other hand, neither CME1 nor CME2 seem to be a promising candidate to be the source of the superstorm, being able to produce, at most, a glancing blow on the Earth's magnetosphere (Paper II).

According to three reconstructions of the MC responsible for the geomagnetic superstorm (Yurchyshyn, Hu, and Abramenko, 2005; Möstl *et al.*, 2008; Lui, 2011), its dimensions in the ecliptic plane were < 0.3 AU. This size corresponds to an expansion angle of $< 17°$, which is similar to that of the presumable CME (Paper II). To meet the Earth, the MC expanding in such a narrow angle should be ejected close to the solar disk center. Such a weak expansion is favored, if the MC is disconnected from the Sun. These speculations will be supported in Paper IV.

The observational suggestions and the listed conjectures indicate that the ejection responsible for the superstorm probably originated during the E4 burst. The formation of the ejection started at E4A at a height of about 100 Mm ($\approx 0.14 R_\odot$) and was completed by the end of E4D. The latter is supported by the appearance of the central brightening in region AR 503 (Figure 2e). A possible height, at which the formation was completed, is of the order of $V_{\rm transit} \times \Delta t_{\rm E4} \approx 1.7 R_\odot$, with $\Delta t_{\rm E4}$ being the duration of burst E4, and $V_{\rm transit} \approx 800-900$ km s^{-1} being an average Sun–Earth transit speed of the ICME (estimated from the decrease of the Dst index on 20 November). This height can be overestimated by a factor of 2–3 due to the uncertainties in the velocity as the CME can accelerate as it leaves the Sun and decelerate during its transit away from the Sun. A probable height, at which the formation was completed, is therefore between $0.6 R_\odot$ and $1.7 R_\odot$.

It is difficult to expect to have direct observations of the processes, which occurred at the heights previously estimated close to the solar disk center. Therefore, we are forced to involve indirect observational indications and calculations. We use the observational indication provided by the evolution of the dimming regions D1–D3 in Figure 3. Their configuration is visible in the EIT 195 Å difference image shown in Figure 3a. The time profiles of the average brightness in selected regions having the lowest intensity and longest lifetime are presented in Figure 3b. Unlike Attrill *et al.* (2007), who defined a dimmed region as the brightness decrease below the quiet-sun brightness level (the horizontal line in Figure 3b), we select the dimmings simply by a decrease of the brightness with respect to the pre-event level. Our different selection criterion indicates that we are considering a different kind of phenomenon.

Most likely, the major cause of a dimming (in our definition) is the density decrease in the coronal structures due to their expansion. The brightness in the extreme-ultraviolet (EUV) and soft X-ray images is proportional to the column emission measure. The brightness, I, of an expanding closed coronal structure of a linear size, L, and area, $A \propto L^2$, filled with a fixed total number of emitting particles, N_0, should be $I \propto EM/A \propto n^2 L = (N_0/V)^2 L \propto 1/L^5$. Thus, the expansion alone should result in a considerable brightness decrease and a strong pressure gradient, which causes a secondary subsonic plasma outflow in the footprint regions of a CME (Harra and Sterling, 2001; Imada *et al.*, 2007;

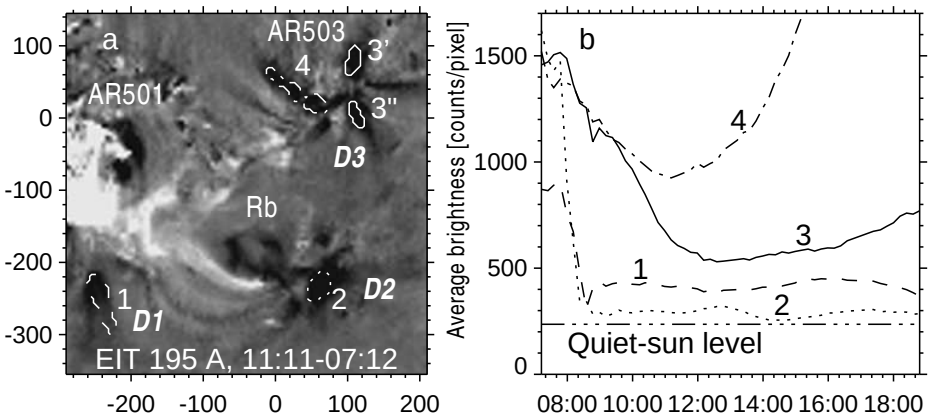

Figure 3. Dimming regions near the solar disk center well after the event. (a) The configuration of dimmings in the EIT 195 Å difference image. Five significantly dark and long-lived dimmed regions are selected using contours of different line styles. The solar rotation is compensated to 08:20 UT. The axes are in arc seconds from the solar disk center. (b) Time profiles in separate dimmed regions. Labels 1 – 4 denote the corresponding regions in panel (a); the styles of the lines in panel (b) and the corresponding contours in panel (a) are the same. The time profile 3 is averaged over regions $3'$ and $3''$. The horizontal line presents the average quiet-sun intensity level in the EIT 195 Å images, two of which were used for the difference in panel (a).

Jin *et al.*, 2009). On the one hand, the outflow is responsible for the redistribution of the coronal plasma from footprints into the expanding volume. On the other hand, due to the subsequent plasma supply from the chromosphere-to-corona transition region, the outflow probably becomes the major factor to recover the brightness in the dimmed regions. This simple consideration also explains why the development of dimming is often observed to start before the eruption, when coronal structures gradually expand during the initiation phase.

The time profiles in Figure 3b show that different parts of the star-like dimming D3 recovered considerably faster than the long-lived dimmings D1 and D2. The analysis of the magnetic connectivity shows that the plage region, where dimming D2 occurred, was connected to AR 503 associated with dimming D3. In addition, a fan of long diverging field lines rooted in the plage region connected it to remote regions far to the South–West. Possibly, D2 shared a footprint of CME2 and had therefore the time profile typical of long-lived core dimmings. The pronouncedly shorter lifetimes of regions $3'$, $3''$, and 4 of the atypical dimming D3 hints at its involvement into an eruption, in which a structure disconnected from the Sun developed. The disconnection produced a stretched magnetic loop. Its subsequent evolution is determined by the relation between the magnetic tension, which tends to shrink the loop, and the opposite influence of the plasma pressure and the plasma outflow responsible for the dimming in its bases. The shrinking duration for the loop with a length of $L \sim 1.7R_\odot \approx 10^3$ Mm is presumably comparable to the time required to stop the plasma outflow, $\Delta t \sim L/C_S \sim 10^4$ s ($C_S \sim 10^2$ km s^{-1} is a mean sound speed of the plasma outflow originating from the low corona up to the chromosphere-to-corona transition region). This estimate is of the order of the observed formation time of dimming D3.

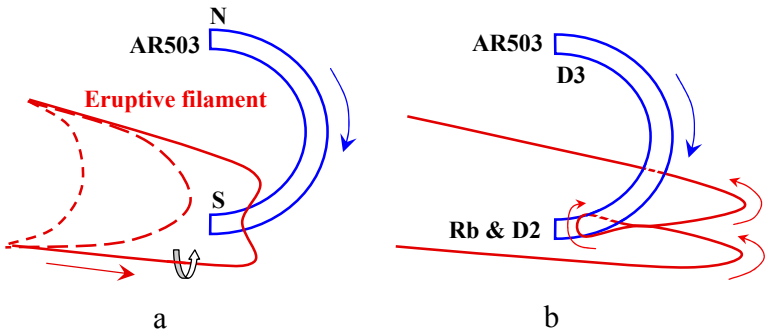

Figure 4. Presumable interaction between the eruptive filament (red) and a static coronal structure (blue) suggested by the observational hints. The static structure connects the N-polarity of AR 503 with an S-polarity plage region and region of bifurcation Rb. The arrows indicate the directions of the axial magnetic fields. The curled arrow indicates the direction of the poloidal flux in the filament. (a) The onset of the interaction. (b) Subsequent expansion of the eruptive filament. The interaction results in the development of dimmings D3, D2, and at the former position of Rb.

Figure 4 summarizes the listed observational indications of a possible interaction between the eruptive filament (red) and a large static coronal structure (blue). One of its ends is rooted in AR 503, and the opposite-polarity basis corresponds to a plage region and region of bifurcation, Rb. The onset of the interaction and bifurcation of the filament in shown in Figure 4a. In a subsequent expansion of the eruptive filament in Figure 4b, its top brakes at the blue structure, while its lateral portions stretch out in a Y-like form. In response to the interaction, dimmings develop in the plage region (D2) and Rb as well as dimming D3 at the opposite end of the blue structure rooted in AR 503. Most likely, the eruptive filament was far from AR 503 (*cf.* Figures 2 and 3), which nevertheless appears to be implicated. We shall use this presumable scheme as a hint in our considerations.

2.2. Analysis Techniques

A major step in our study is the analysis of the coronal magnetic field *via* the extrapolation of photospheric magnetograms. For AR 501 we have a vector magnetogram that makes possible a non-linear force-free (NLFF) field extrapolation within its field of view, $315'' \times 315''$. However, the region of interest, including Rb, D2, and D3 in Figure 3a, is far West from the vector magnetogram. The only possible way to analyze a larger region is a potential extrapolation of the full-disk SOHO/MDI magnetograms (Scherrer *et al.*, 1995). The potential approximation is usually considered to be insufficiently accurate to describe realistic configurations under the presence of significant electric currents. Nevertheless, in Paper I we have used it successfully to visualize the filament, its height, and the topological discontinuity, whose presence accounted for the apparent disintegration of the eruptive filament. Let us try to check, how realistic the results of the potential extrapolation are by comparing them with real coronal loops in EUV images.

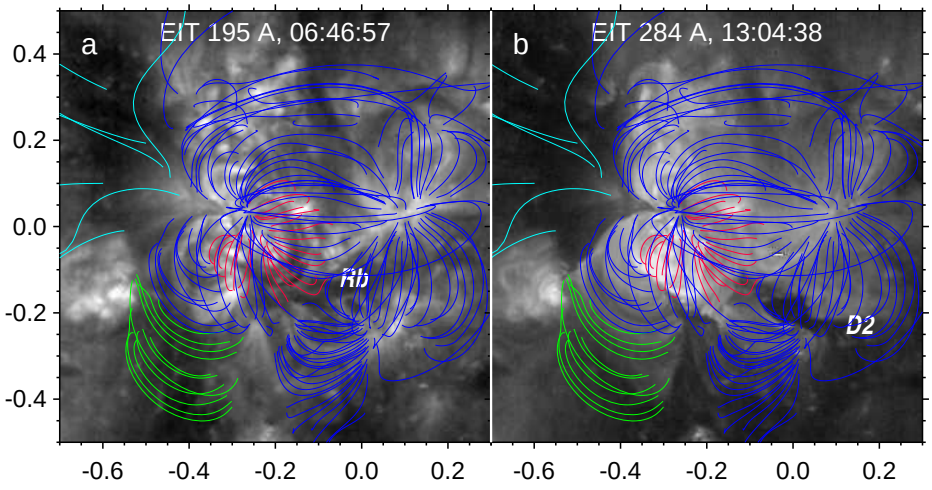

Figure 5. Extrapolated field lines overlaid on: (a) a pre-event EIT 195 Å image and (b) a post-event EIT 284 Å image. All data were taken on 18 November. The MDI magnetogram at 09:35 UT was used for the potential extrapolation. The EIT images are corrected for the solar rotation to this time. The axes are in solar radii from the solar disk center.

Figure 5 compares the field lines computed in the potential approximation, using the method and package of Rudenko and Grechnev (1999) and Rudenko (2001) for the full-disk SOHO/MDI magnetogram observed on 18 November at 09:35 UT. The spatial resolution is determined by 90 spherical harmonics. The starting points for all of these field lines were chosen manually, and their density does not correspond to the real magnetic field strength distribution. The correspondence between the computed field lines and the visible coronal loops is what is relevant to us.

Figure 5a presents the EIT 195 Å image observed before the event in gray scale overlaid with a few sets of computed magnetic field lines. The same sets of the field lines are overlaid on the post-event EIT 284 Å image in Figure 5b. The red lines embrace the pre-eruptive filament F1. The light-blue lines correspond to open magnetic field lines rooted in the coronal hole East of AR 501. The green lines cover a southern filament channel; the corresponding coronal loops appeared after the event in Figure 5b. All other structures are traced by the blue lines.

Although a one-to-one correspondence is not observed, as expected, the figure shows an acceptable similarity of the computed blue field lines to the structures in the EUV images. The pre-event EIT 195 Å image in Figure 5a presents rather short loops reaching small heights. The computed field lines correspond to the loops diverging from AR 503 and from the plage region slightly South–West of Rb. The overall correspondence in shapes and directions between the computed and real structures is observed to the South–East and North–East of AR 501. The red field lines above the filament correspond to magnetic structures, which are expected to be seen but are not visible. These lines fairly correspond to the post-eruption arcade to the South of AR 501 in Figure 5b. The light-blue open field lines are not expected to be visible.

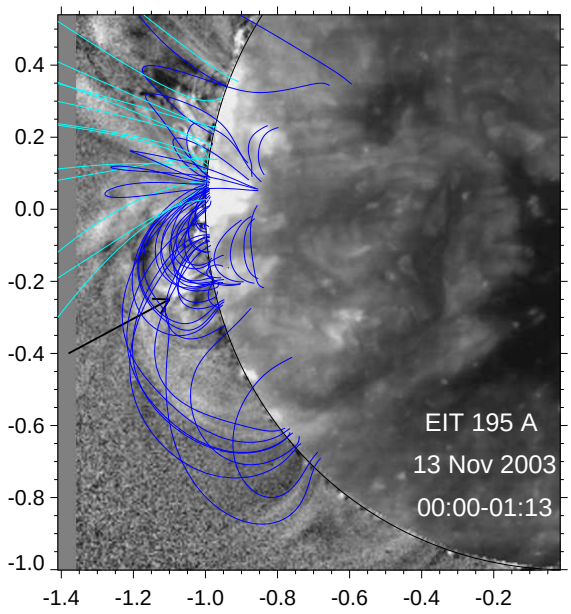

Figure 6. Comparison of the field lines computed in the potential approximation for the MDI magnetogram produced at 09:35 UT on 18 November with a synthetic EUV image composed from EIT 195 Å images actually observed on 13 November. The black arrow indicates the position of the topological discontinuity as it was on 18 November. The axes are in solar radii from the solar disk center.

The post-event EIT 284 Å image in Figure 5b shows somewhat higher loops. For example, connections between AR 501 and AR 503 become detectable here. In addition to the mentioned features, note that region Rb is not seen here. Dimming D2 resembling a transient coronal hole has decreased in size with respect to its appearance in Figure 3.

We cannot observe in these images the structures, which reach still larger heights, because of their lower brightness (due to a lower plasma density) against the brighter lower loops. They can only be detected against the sky on the limb. However, the on-limb magnetogram is very uncertain. We therefore have computed the field lines extrapolated from the magnetogram observed on 18 November at 09:35 UT and rotated them to 13 November. This day was characterized by ongoing activity on the East limb. We have built a composed off-limb EUV image from the ratios of several EIT 195 Å images observed from 00:00 UT to 05:00 UT, bypassing the intervals of activity. The on-disk part is an average of six EIT 195 Å images observed from 00:00 UT to 01:13 UT, in which the solar rotation was compensated. The result is presented in Figure 6. The light-blue lines correspond to the open field. In spite of the five-day difference and active conditions, there is an overall correspondence between the calculated field lines and the off-limb structures.

In summary, Figures 5 and 6 demonstrate that the extrapolation in the potential approximation presents a more or less realistic picture. Furthermore, we observe that despite the ongoing activity, the distribution of coronal magnetic field remained relatively stable.

3. The Magnetic Helicity Issue

3.1. Suggestion of Chandra *et al.* (2010) in Terms of a Simple Eruption Preserving Helicity

Chandra *et al.* (2010) computed the maps of the magnetic helicity flux density injection and, in spite of the mixed helicity signs, showed the existence of a localized positive helicity injection in the southern part of AR 501. They also concluded that the positive helicity was ejected from this portion of the AR leading to the observed positive-helicity MC. The accumulated positive helicity, as Chandra *et al.* (2010) considered, was concentrated in one of the portions of the pre-eruptive filaments, while the helicity of other portions was negative and corresponded to the sign of the global helicity of AR 501.

However, the idea of Chandra *et al.* (2010) to account for the positive helicity of the near-Earth MC does not seem to be convincing. Firstly, the helicity injection rate measured for some part of an active region during a rather short time interval does not provide information on the total helicity accumulated during the preceding evolution. Secondly, the fresh idea of the authors about the presence of the opposite-helicity portions in the body of the pre-eruptive filament, in our opinion, does not have a convincing visual support. Finally, Chandra *et al.* (2010) pointed out that the injection rate of the positive helicity flux was not high, so that such an injection was able to accumulate the helicity appropriate for the MC in, at least, six days.

3.2. Absence of Positive Helicity in the Source of the Major Eruption

Chandra *et al.* (2010) used the orientation of the filament barbs as a morphological indication of a section with a positive twist in the pre-eruptive filament (Figures 1a and 1b). These authors found a filament segment consisting of two sections, which had the same direction of the central axis, but opposite twists. The authors indicated, however, that this determination was relatively ambiguous. In our opinion, the identification of the filament barbs and their usage as a morphological indication is questionable for such a broad filament. According to Paper I, the filament was tilted by about 60° to the solar surface, and features as the filament barbs could correspond to different parts located at different heights (see Figures 14 and 17 from Paper I).

To confirm the suggestions inferred from the apparent filament barbs, Chandra *et al.* (2010) invoked different methods, *i.e.*, magnetic field extrapolation based on the linear (constant α) force-free field approximation, and the computation of the magnetic helicity flux density injection. Using a magnetogram before the eruptions (at 06:23 UT), they found a dominant negative α by matching the shapes of the computed field lines to that of the observed coronal loops. This finding confirms their conclusion that the large-scale magnetic field of AR 501 had a negative helicity sign. The authors also compared the computed field lines with the post-flare arcade loops in the TRACE 171 Å full-resolution image (Handy *et al.*, 1999) at 09:43 UT and found that the loops could be modeled by using any small α value — positive, or negative, or null. They also found that,

despite the predominance in the AR 501 of negative α values, corresponding to the negative global magnetic helicity, a small α tended to be positive in the southeastern part of the AR. The authors also computed an ongoing injection of the positive-helicity flux in this part of AR 501 and conjectured that this localized injection could be sufficient to make the magnetic helicity positive in this area, but its total value remained uncertain.

Yurchyshyn, Hu, and Abramenko (2005) modeled the post-flare loops visible in a half-resolution 195 Å image obtained with EIT at 09:36 UT and found that the best value of α was slightly positive along the total length of the visible arcade. This led them to a conclusion that the AR had a global positive magnetic helicity. The authors used the images obtained at the late post-flare stage, when the non-potentiality of the post-flare loops was least pronounced being, therefore, difficult to observe. On the other hand, at the earlier stages of a flare, more favorable in this respect, the loops are usually unresolved because of their small size. We have succeeded in solving this problem.

The loops of a compact arcade visible in the TRACE images in Figures 7a–7c (not analyzed by the aforementioned authors) are skewed counter-clockwise in sunspot N3 and the region around it, indicating negative helicity. The skewness of the loops in region S4 considered by Chandra *et al.* (2010) seems to be the same, as expected for both ends of the same loops, connecting these regions in Figures 7a–7c. The whole flare arcade has an inverse S-shape, which also corresponds to negative helicity.

To verify this suggestion, we have computed the current helicity, $h_c = \mathbf{B} \cdot (\nabla \times \mathbf{B})$, from a vector magnetogram of AR 501 observed at *Big Bear Solar Observatory* (BBSO) on 18 November at 20:26 UT (courtesy V. Yurchyshyn). The field of view of the magnetogram, of $315'' \times 315''$, was centered near the N1 sunspot (about $[-300'', +20'']$ at 08:00 UT) and covered the active region and its vicinity, but did not reach the region of bifurcation. The line-of-sight component in the BBSO magnetogram was considerably saturated in sunspots S1, N3, and S3. Our computations were carried out in a spherical box with a photospheric base of $22^\circ \times 22^\circ$ and a height of 135 Mm from both the raw magnetogram and a saturation-corrected one by using a temporally close SOHO/MDI magnetogram. We used the method of the NLFF extrapolation (Rudenko and Myshyakov, 2009) to compute two kinds of the current helicity maps. The first kind of map, the photospheric h_c density map, presents the distribution of h_c at the photospheric layer. The second kind of map is the column density distribution of h_c. Each pixel of such a map is the photospheric base of a vertical column, whose height is 135 Mm, and presents the total h_c over all cells constituting this column. Comparison of the maps of the two kinds show that they are not very different, because the major contribution to the total current helicity is due to the lowest layers closest to the photosphere.

Each attempt has resulted in a significant excess of the negative helicity in both the whole active region and in the framed area considered by Chandra *et al.* (2010), but with somewhat different quantitative results. The saturation-corrected current helicity map is shown in Figure 7d. The ratios of the total negative to positive helicity for both the photospheric layer and for the total volume are specified in the gray boxes. The top left box presents the ratios for the whole

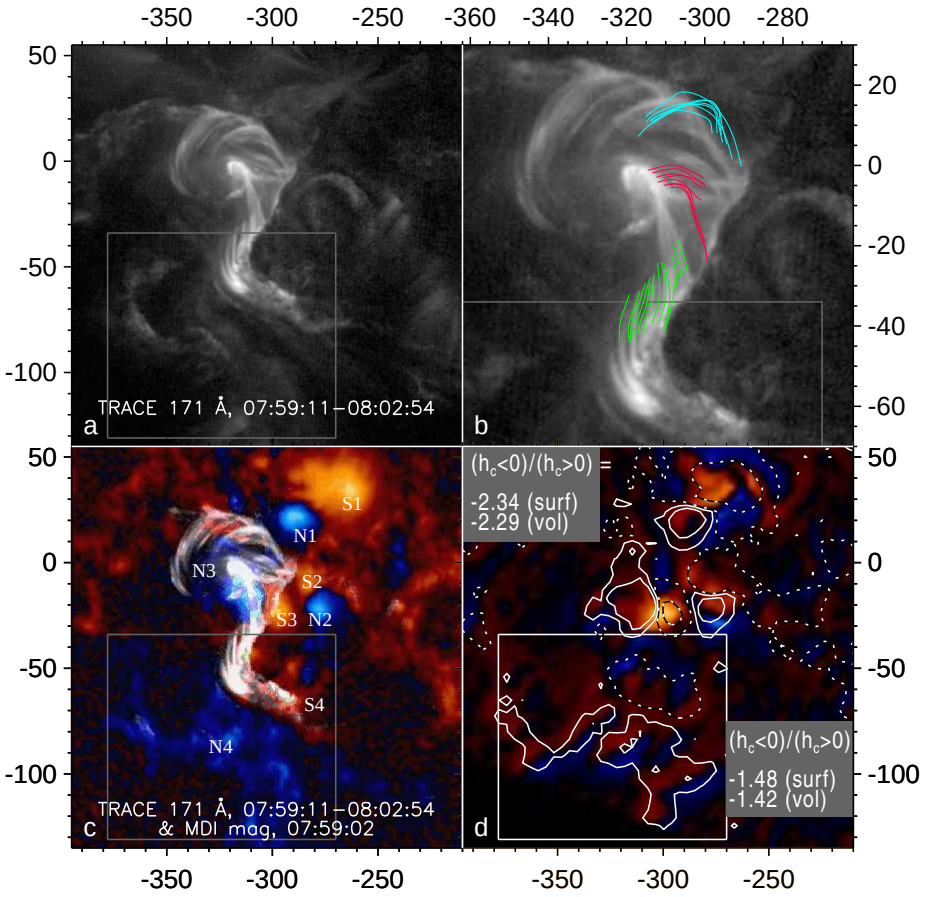

Figure 7. The magnetic helicity sign issue. (a) Inverse S-shaped arcade in a TRACE 171 Å composite image. The region analyzed by Chandra *et al.* (2010) is framed in all panels. (b) Enlarged image of the arcade overlaid with magnetic field lines calculated from the NLFF extrapolation. (c) Combination of the TRACE image in panel (a) with an MDI magnetogram (N-polarity blue, S-polarity red, numbering according to Chandra *et al.*, 2010). (d) Current helicity map computed from the NLFF extrapolation. Each pixel of this map is the photospheric base of a vertical column as high as 135 Mm. The red- (blue-) shaded regions correspond to the values of negative (positive) current helicity within the volume of this column. The contours outline the negative (dotted, $-(120, 600)$ G) and positive (continuous, $+(30, 250)$ G) B_z polarities in the BBSO magnetogram used in the computations. The top left gray box presents the ratio of the total negative to positive current helicity at the photospheric layer (surf) and in the coronal volume (vol) for the whole region. The bottom right gray box is related to the framed region. The axes are in arc seconds from the solar disk center.

region, the bottom right box is related to the framed region. Indeed, the excess of the total negative helicity is less in the framed region, in agreement with the ongoing injection of the positive helicity found by Chandra *et al.* (2010), but still insufficient to make the total helicity in this region positive. The absence of positive magnetic helicity in the localized area of AR 501 also indicates the absence of segments with the corresponding handedness in the body of the main

filament F1. Note also that the central part of the inverse S-shaped structure in Figures 7a and 7b passes between sunspots N3 and S3, where the negative current helicity is the largest in the whole AR 501.

To make the situation clearer, we have additionally calculated magnetic field lines from the same NLFF extrapolation, which was used in the computation of the current helicity. It is difficult to reach a perfect correspondence between the field lines and the observed loops, because the rapid evolution of AR 501 during the 12.5 hours separating the EUV image and the vector magnetogram could imply a change in the small-scale features, while the strong saturation of the vector magnetogram (and, to a lesser degree, its limited field of view) could considerably affect long loops. For example, we have not succeeded to reproduce the long loops in the North–East part of the arcade; however, its negative helicity is undoubted. Nevertheless, three sets of field lines with $\alpha < 0$ overlaid on the enlarged image of the arcade in Figure 7b more or less correspond to the actually observed loops, in particular, the green lines overlapping the region of the questionable handedness.

All of these circumstances show that the attempts to reconcile the handedness of the magnetic cloud and active region 501 are not promising. The question how the right-handed MC could be formed in the eruption of the left-handed filament remains unanswered.

3.3. Eruptions with Mismatching Helicity Sign

The scenario proposed by Chandra *et al.* (2010) corresponds to the concept of a simple eruption, when the internal magnetic helicity of a pre-eruptive structure, *i.e.*, its self-helicity (or twist helicity), $H_{\rm m}^{\rm self}$, determines the helicity sign of the interplanetary MC. Probably, this situation is typical of CMEs associated with eruptions of quiescent filaments outside active regions. However, if a filament (flux rope) erupts from an active region, then, under certain circumstances, the helicity of the MC can have a different origin. This scenario implies the interaction and reconnection between magnetic fields of the eruptive structure with coronal magnetic fields surrounding the parent AR. In such a case, a new magnetic structure is formed, which is the progenitor of the future interplanetary MC. Its helicity is determined by the sum of $H_{\rm m}^{\rm self}$ and the mutual (or linkage) helicity, $H_{\rm m}^{\rm mut}$, of the interacting magnetic fluxes. *Via* magnetic reconnection, the mutual helicity is transformed into the self-helicity of the MC. Depending on the sign of $H_{\rm m}^{\rm mut}$ and the value of the $H_{\rm m}^{\rm mut}/H_{\rm m}^{\rm self}$ ratio, the MC helicity can be different from the pre-eruptive structure not only in the value, but also in the sign. Such eruptions with mismatching helicity were suggested in the study by Leamon *et al.* (2004); this scenario is also supported by the observations of the apparent disintegration of eruptive filaments mentioned in Section 1.

To understand what could happen on the Sun on 18 November, we first analyze the configuration of the magnetic field on spatial scales considerably larger than the size of the vector magnetogram in Figure 7. This is possible by using full-disk magnetograms, of which line-of sight measurements (*e.g.*, by SOHO/MDI) are only available for 2003. Thus, we had to use for this purpose MDI magnetograms and the potential field extrapolation.

4. Large-Scale Coronal Magnetic Configuration around the Left-Handed Eruptive Filament

The coronal field in a magnetic complex consisting of regions 501, 503, and their environment was computed in the potential approximation using the mentioned package (Rudenko and Grechnev, 1999; Rudenko, 2001) for the full-disk SOHO/MDI magnetograms of 18 November observed at 06:23, 07:59, and 09:35 UT. The computations used 90 spherical harmonics. The field line distribution computed from each of the magnetograms was similar; we mainly use here the magnetogram at 09:35 UT. Figures 8–12 present the coronal magnetic configuration. The S–N–S–N quadrupole in Figures 8, 10, and 12 is its basis. Figure 10 shows that the major eastern S-polarity sunspot has a large excess of negative magnetic flux which is unbalanced in this quadrupole. A considerable portion of this flux is connected to remote sites on the solar surface (Figure 12) separated from AR 501 by the global polarity inversion line.

4.1. Magnetic Null Point and Region of Bifurcation of the Eruptive Filament

A topological particularity of the coronal configuration is a magnetic null point located at a height of about 100 Mm above the photosphere. This is the only null point associated to large-scale magnetic fields on the visible side of the Sun. Figure 8 shows a side view of the complex of regions 501, 503, and their surroundings. This complex was located at the solar disk center on 18 November. Figure 8a shows the location of the null point (slanted cross) inside this complex, the pre-eruptive U-shaped filament F1 (red semicircular arrow), and region of bifurcation Rb, which had well-pronounced counterparts on the solar disk visible in the Hα line and in soft X-rays (see Paper I). Figure 8b shows the magnetic field lines, which pass close to the null point. According to the classification of Parnell *et al.* (1996), here we are dealing with a negative improper three-dimensional null point with the fan field lines rooted in the N polarities, and the field lines around the spine rooted in the S polarities. The fan is perpendicular to the spine.

The region of bifurcation Rb is rather close (but not exactly co-spatial) to the site, where the spine field line, which leaves the null point, enters the photosphere. The lack of coincidence in our extrapolation, besides their possible actual difference, can be due to: a) the usage of the potential approximation, and b) the insufficient spatial resolution because of the limited number of the spherical harmonics. There are indirect indications of a connection between Rb and the null point:

1) Rb firstly appeared as an isolated bright point in the Hα and SXI images one minute later than the U-shaped filament started to move at 07:41 UT. The Rb region and the filament were not connected by field lines. Their connection is possible *via* reconnection at the magnetic null point located between them. Invoking magnetic reconnection with a possible transformation of the null point into a current sheet is not the only possibility here. The MHD disturbances generated by the initial displacement of the eruptive filament can cause local plasma heating in the vicinity of the null point by the accumulation and dissipation of

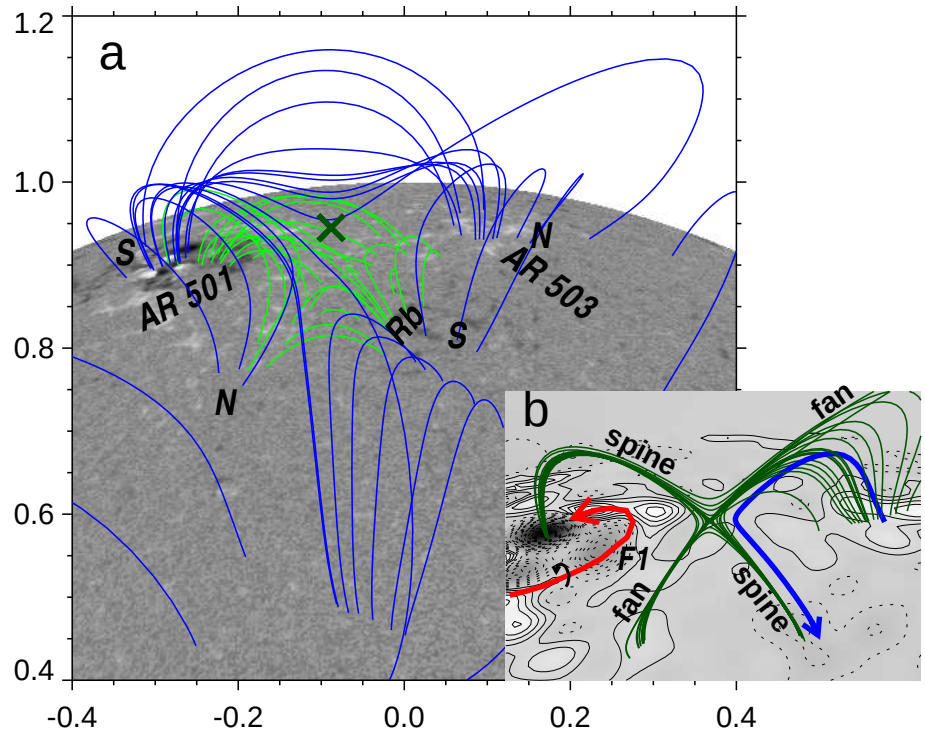

Figure 8. Side view of the coronal magnetic configuration around the pre-eruptive filament computed from the SOHO/MDI magnetogram of 18 November, 09:35 UT. (a) Field lines in the large-scale environment of the magnetic null point denoted with the dark-green slanted cross. (b) A selected set of field lines passing close to the magnetic null point shown in the same scale as in panel (a). The null point at their apparent intersection corresponds to the dark-green slanted cross in panel (a). The thick red arrow represents the pre-eruptive filament and the direction of its axial field. The small black circular arrow around it indicates its negative handedness. The blue arrow represents the connectivity of the west N–S dipole, which is a part of the S–N–S–N quadrupole. The relative position of the red and blue arrows suggests a positive handedness. The contour levels of the radial magnetic component are symmetric relative to zero in steps of 31 G: dotted $-(15, 46, ...728)$ G, continuous $+(15, 46, ...139)$ G. The axes are in solar radii from the solar disk center.

the energy of fast-mode MHD waves or Alfvén waves along the spine (see, *e.g.*, the review by McLaughlin, Hood, and de Moortel, 2011; Afanasyev and Uralov, 2012). Such heating augments the flux of heat and, possibly, that of non-thermal particles responsible for the increase of the emission intensity from the chromospheric and coronal plasmas above the photospheric base of the spine field line.

2) The Rb region has appeared as a small ring with a brightening running clockwise (Paper I) at the same time as the eruptive filament F1 would pass the magnetic null point (this phenomenon started at 08:08 UT). A similar situation with a considerably larger ring was observed in an eruptive event of 1 June 2002 (Meshalkina *et al.*, 2009). In that event, the magnetic configuration was different, it had a funnel-like shape, and the ring was situated above the photospheric footprint of a hemispheric separatrix surface with a magnetic null at its top. The

'magnetic funnel' confined all the ejections, as suggested by the movies of the event. Similar to our case, a brightening running along the ring was observed in the 1 June 2002 event, when the eruptive filament, being transformed into a rotating ejection, passed through the magnetic null. The motion of this ejection through the null must be accompanied by reconnection of the magnetic field lines associated to the ejection with those on the separatrix surface or nearby. A response to this process was a concurrent EUV disturbance, which propagated along the ring-like footprint of the separatrix surface.

In the 18 November 2003 event, the ring structure of region Rb could be a manifestation of the photospheric base of a bundle of magnetic field lines twisting around, or close to the spine field line. The twist indicates the presence of the longitudinal electric current along the spine and the inadequacy of the potential field approximation, which we use. The twist is necessary for the brightening running along the ring that accompanies the concurrent magnetic reconnection of this bundle with an arbitrary magnetic rope or eruptive filament, for example, with a cylindrical shape. A scheme in Figure 9 illustrates the interaction. As this Figure shows, the bundle should be similar to a non-uniformly twisted cylindrical flux tube to produce a running brightening. The Gold–Hoyle uniformly twisted tube with a non-constant α does not satisfy this condition, while the Lundquist magnetic cylinder with a constant α satisfies it. Since Rb is located within the zone of the negative magnetic polarity, the clockwise-running brightening corresponds to $\alpha < 0$. In turn, this indicates that the self-helicity of the magnetic flux around the spine is most likely negative.

3) In the 1 June 2002 event (Meshalkina *et al.*, 2009), the interaction of the ejection with the magnetic 'funnel' and its passage through the null appeared to have produced a wave disturbance in the corona observed as an 'EIT wave' rapidly expanding above the limb. In the 18 November 2003 event, the bifurcation of the eruptive filament was also accompanied by the appearance of a coronal wave, whose kinematical center was located high in the corona, above Rb (Paper II). This was the second wave, not expected in the event. The kinematical center of the first wave was within AR 501 and corresponded to the impulsive acceleration stage that is typical of impulsive eruptions (Grechnev *et al.*, 2011b).

4.2. Positive Mutual Helicity of the Filament and West Dipole

Until now, the contribution to the MC magnetic helicity from the relative position of the pre-eruptive filament and the structures outside of AR 501 have not been taken into account. These structures got in contact at the magnetic null point, toward which the top of the expanding filament F1 moved. Figure 8 illustrates the positions of the structures which could be involved in the eruptive process. The values of the fluxes belonging to the West, East, North, and South magnetic dipoles are not known *a priori*. Note that each dipole represents only a fraction of the magnetic flux of a corresponding magnetic domain within the quadrupole configuration in Figure 8. It is also not known if the interaction between any of these dipoles and the eruptive filament was significant. Let us estimate by linking with which of these dipoles the pre-eruptive filament had the largest positive mutual helicity.

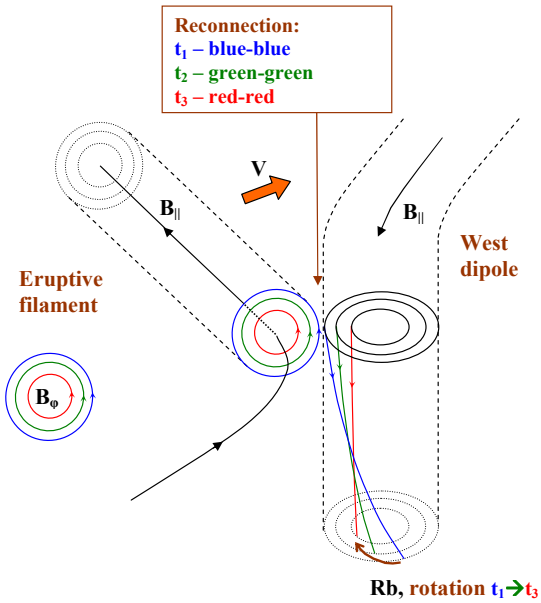

Figure 9. Interaction of the eruptive flux rope (left) and a non-uniformly twisted bundle (right) of magnetic field lines belonging to the West dipole and rooted in Rb. Their normal cross-sections are shown to be orthogonal in the place of interaction. The orange thick arrow indicates the direction of motion of the flux rope. The field lines sequentially involved in magnetic reconnection at times t_1, t_2, and t_3 are denoted with the colors presented in the top rectangle. Magnetic reconnection leads to a concurrent brightening running clockwise in the chromosphere and low corona above the Rb region (the brown round arrow at the bottom). The axial magnetic fields, $B_{\|}$, of the eruptive flux rope and the bundle correspond to the positions of the thick blue and red loops at t_1 in Figure 14a, respectively.

The presence of the positive mutual helicity is suggested by Figure 8b. The curved blue arrow in the figure indicates the direction of the magnetic flux in the West dipole. The red arrow indicates the direction of the axial magnetic field in the pre-eruptive filament. Let us invoke the right-handed screw rule and direct the screw axis along the blue arrow at its descending spine portion; then the right-handed direction corresponds to the direction of the red axial field in the top of the filament. If we put the screw axis along the top of the filament, then the result is the same; the descending part of the blue arrow rotates clockwise. Therefore, one might expect that the West dipole and the pre-eruptive filament constitute a right-handed system.

To estimate the mutual magnetic helicity, $H_{\rm m}^{\rm mut}$, we use the technique of interior angles (Berger, 1998; Démoulin, Pariat, and Berger, 2006). For this purpose we need a top view of the magnetic configuration presented in Figure 8b. Such a view is shown in Figure 10, which represents the complex of regions 501, 503, and their environment located almost at the solar disk center when viewed from Earth. The dotted lines $D_{\rm N}$, $D_{\rm S}$, $D_{\rm E}$, and the blue vector $\mathbf{D}_{\rm W}$ connect the positive and negative footpoints of the magnetic fluxes in the North, South, East, and West magnetic dipoles. The red vector **F1** connects the western (negative)

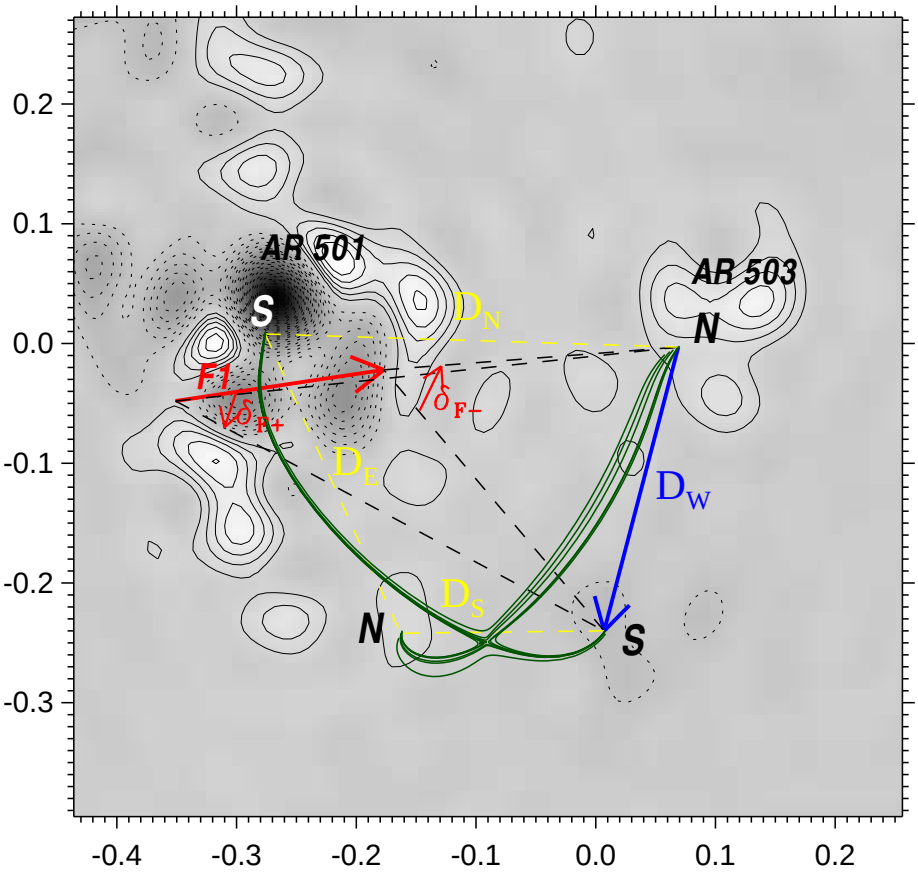

Figure 10. Top view of the magnetic configuration presented in Figure 8. The red vector **F1** connects the photospheric bases of the erupted portion of the filament in AR 501. The yellow dashed lines $D_{\rm N}$, $D_{\rm S}$, $D_{\rm E}$, and the blue vector $\mathbf{D}_W$ connect the photospheric bases of the North, South, East, and West magnetic dipoles. $\delta_{\rm F1+}$ and $\delta_{\rm F1-}$ are the angular spans of vector $\mathbf{D}_{\rm W}$ measured from the ends of vector **F1**. The axes are in solar radii from the solar disk center. The contour levels are symmetric relative to zero in steps of 35 G; dotted $-(35, 70, ...805)$ G, continuous $+(35, 70, ...175)$ G.

and eastern (positive) ends of the erupted portion of the filament. The sign of $H_{\rm m}^{\rm mut}$ depends on the relation between the height $h_{\rm F1}$ of the pre-eruptive filament and those of the magnetic loops, $h_{\rm N}$, $h_{\rm S}$, $h_{\rm E}$, and $h_{\rm W}$, which constitute each of the dipoles. The estimation shown below corresponds to the real case in which the height of the pre-eruptive filament is less than any of the other magnetic loops. For example, the mutual magnetic helicity of filament F1 and the West dipole $\mathbf{D}_{\rm W}$ is:

$$H_{\rm m}^{\rm mut}({\rm F1,\ W}) = \Phi_{\rm F1}\Phi_{\rm W}(\delta_{\rm F1^+} + \delta_{\rm F1^-})/180^\circ \approx +\Phi_{\rm F1}\Phi_{\rm W}/10 > 0,$$

where the angles δ are positive counter-clockwise, so that $\delta_{\rm F1^+} = -33^\circ$ and $\delta_{\rm F1^-} = +51^\circ$. The flux of the axial magnetic field in the pre-eruptive filament, $\Phi_{\rm F1}$, is unknown. The magnetic flux of the West dipole, $\Phi_{\rm W}$, will be estimated in Section 4.3.

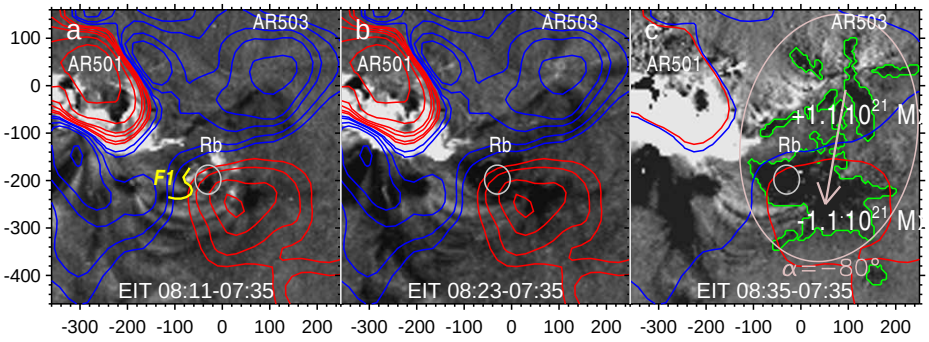

Figure 11. Manifestations of a presumable eruption at the solar disk center around 08:14 UT shown by the development of dimmings in EIT 195 Å images overlaid with the contours of the coronal B_r magnetogram extrapolated from an MDI magnetogram at a height of 28 Mm (blue N-polarity, red S-polarity). The contour levels are $\pm(2.5, 5, 10, 15, 30, 60)$ G in panels (a) and (b) and ± 2.5 G in panel (c). The yellow contour in panel (a) outlines the leading edge of the eruptive filament pouncing on a coronal obstacle above the bifurcation region Rb denoted by the small oval. The green contours in panel (c) outline the darkest dimming areas, which overlay a dipole outlined with a large oval. The arrow shows the direction of the resulting magnetic field in the dipole.

The mutual helicities $H_{\rm m}^{\rm mut}\{({\rm F1, S}); ({\rm F1, E}); ({\rm F1, N})\}$ can be estimated in a similar way. In particular, $H_{\rm m}^{\rm mut}({\rm F1, E}) < 0$. Next, the angles between the lines F1, $\mathbf{D}_{\rm N}$, and $\mathbf{D}_{\rm S}$ in Figure 10 are small; therefore, $H_{\rm m}^{\rm mut}({\rm F1, S}) \gtrsim 0$ and $H_{\rm m}^{\rm mut}({\rm F1, N}) \lesssim 0$. Small changes of their mutual orientations can change the signs of the corresponding mutual helicities.

Thus, $H_{\rm m}^{\rm mut}({\rm F1, W})$ appears to be the only solar source for a significant positive magnetic helicity of the interplanetary magnetic cloud. If so, then the magnetic flux of the West dipole should be involved in the eruption of the U-shaped filament F1. This conjecture is confirmed observationally by the development of the double dimmings in the conjugate footpoints of the loops anchored in the West dipole (see Section 4.3).

4.3. Double Dimmings in the West Dipole

Figure 11 presents the development of dimming around 08:14 UT in association with the main eruption on 18 November. The gray scale background in the panels shows three fixed-base ratios of EIT 195 Å images, ${\rm Ratio}_j = {\rm Image}_j/{\rm Image}_1$. The contours outline the positive (blue) and negative (red) modeled flux concentrations of the coronal B_r magnetogram. Here B_r is the radial component of the coronal magnetic field computed at the spherical surface with a radius $R_{\rm mag} = 1.040 R_\odot$ (*i.e.*, at a height of $h_{\rm mag} = 28$ Mm above the photosphere) from the SOHO/MDI magnetogram observed at 07:59 UT.

Figure 11a presents the collision of the eruptive filament F1 (yellow) with a high coronal structure. Their interaction is indicated by the brightenings turning around the bifurcation region (Rb) underneath (see Paper I). A large dimming South of AR 501 resulted from a preceding eruption and is beyond our scope. Figure 11b (12 minutes later) presents the outcome of the collision. Both the brightenings and region Rb disappeared. Two dimming areas developed instead.

A new large dimming appeared at the previous position of the bifurcation region, and a weaker star-like dimming developed in AR 503. Figure 11c shows the situation observed still 12 minutes later. The green contours outline the darkest portions of the two major West dimming regions.

The star-like dimming in AR 503 and the dimming encompassing the former bifurcation region overlaid a dipole pointing nearly South. The magnetic flux in this dipole probably corresponds to the magnetic flux in a presumable eruptive structure. The value of the magnetic flux computed within the dimming regions depends on the height, $h_{\rm mag}$, to which the magnetogram is related. This can be a photospheric magnetogram actually observed with MDI or a coronal B_r magnetogram computed from the potential field extrapolation. To estimate the magnetic flux in the eruption, we assume that the dipolar double dimming developed mainly due to the stretching of a closed magnetic flux tube, connecting these areas. One might expect that the positive and negative magnetic fluxes within the conjugate dimming areas are equal in absolute value. The equality should be reached at a proper height above the photosphere. At the photospheric level, $h_{\rm mag} = 0$, the computation gives a negative imbalance of the magnetic fluxes, $\Phi^+ = +1.8 \times 10^{21}$ Mx in the star-like dimming and $\Phi^- = -3.9 \times 10^{21}$ Mx in the large South dimming. While the height increases, the imbalance of the fluxes decreases. It becomes zero at $h_{\rm mag} = 28$ Mm, where $\Phi_{\rm dim} \approx \Phi^+ \approx |\Phi^-| \approx 1.1 \times 10^{21}$ Mx, and then becomes increasingly positive. The height at which the flux is balanced is consistent with a typical height range of the coronal emission in the 195 Å line.

Considering each pole of the dipole as the centroid of the magnetic field distribution within each dimming region, we compute an orientation of the dipole of 170° with respect to the North or about −80° with respect to the ecliptic (in the GSE coordinate system). The gray arrow in Figure 11c connects the centroids. The direction of the arrow and its ends acceptably match the blue arrow of the West dipole in Figure 10.

Our previous discussion provides a confirmation of the participation of the West dipole in the formation of the Earth-directed MC with a positive helicity. The estimated magnetic flux, $\Phi_{\rm dim} \approx 1.1 \times 10^{21}$ Mx, is adequate to that in the magnetic cloud near Earth, $\Phi_{\rm MC} \approx 0.55 \times 10^{21}$ Mx, estimated by Möstl *et al.* (2008). The estimated magnetic flux in the West dipole is sufficient for the MC, while the two-fold excess could be lost by reconnection in the interplanetary space as proposed by Möstl *et al.* (2008) and consistent with the fact that the MC crossed the sector boundary of the interplanetary magnetic field. The inclination of the MC to the ecliptic plane estimated by different authors within a range of $\theta = -(49 - 87)^\circ$ (see Möstl *et al.* (2008)) corresponds to the orientation of the West dipole $\alpha \approx -80^\circ$ in Figures 10 and 11c.

5. Formation of the Magnetic Cloud

5.1. Requirements for the MC Formation

According to our analysis in Papers I, II, and IV, the MC hitting the Earth on 20 November had the following characteristics: i) it was formed close to the

solar disk center in the bifurcation of the eruptive filament, ii) it was compact and disconnected from the Sun, and iii) it had an atypical spheromak-like configuration. The outcome of Section 4 suggests that the MC could be formed by the interaction between, at least, two magnetic structures, whose mutual helicity was positive before the eruption. These structures were the West dipole and the pre-eruptive filament. The position of the West dipole on the solar disk meets requirement i).

An additional requirement follows from the total magnetic helicity conservation $H_{\rm m}^{\rm total} = H_{\rm m}^{\rm mut}({\rm F1, W}) + H_{\rm m}^{\rm self}({\rm F1}) + H_{\rm m}^{\rm self}({\rm W})$, where $H_{\rm m}^{\rm self}({\rm F1})$ and $H_{\rm m}^{\rm self}({\rm W})$ are the self-helicities of the pre-eruptive filament and the West dipole, and $H_{\rm m}^{\rm mut}({\rm F1, W})$ is their mutual helicity. The final configuration of the eruption depends on the sign of the total helicity. However, it is not possible to determine the sign of $H_{\rm m}^{\rm total}$ from the analysis of Chandra *et al.* (2010) and our considerations in Section 3.2. The preceding estimates of the helicity sign were related to AR 501 only and did not contain information about the mutual helicity between the filament in the active region and magnetic structures outside of AR 501. The results of Sections 4.2 and 4.3 show that if the magnetic fluxes of the west dipole, $\Phi_{\rm W}$, and the filament, $\Phi_{\rm F1}$, are related as $\Phi_{\rm W} < 10\Phi_{\rm F1}$, then $H_{\rm m}^{\rm total} < 0$ under typical assumptions.

Thus, if the total helicity of two interacting fluxes is transformed through reconnection into the self-helicity of a single eruptive structure, then a right-handed MC cannot be formed. The situation is different, if the interaction and a chain of magnetic reconnections are followed by the formation of two eruptive structures rather than a single one. In this way, redistribution of the magnetic helicity is possible with almost the full transformation of the mutual helicity of two reconnected fluxes into the self-helicity of one of the resulting structures. The second structure can carry away practically the whole negative helicity. The mutual helicity of the two new eruptive structures approaches zero as they separate from each other, and therefore can be neglected.

5.2. Trajectory and Mass Depletion of the Eruptive Filament

As a next step we try to understand: i) the possible geometry of the interaction between the eruptive filament F1 and the magnetic loops in the vicinity of the null point (we associate its projection on the solar disk with the bifurcation region Rb) at their first contact and just after the passage of the null point, and ii) why this interaction was followed by the visible dispersal over the solar surface of the cool plasma, which initially belonged to the eruptive filament F1.

Figure 12 shows a side view of the magnetic configuration, in which the main eruption occurred. For further considerations it is convenient to replace the erupting filament by a magnetic flux rope. The rope has a toroidal (axial) and poloidal (azimuthal) components of the magnetic field. The direction of motion of the middle part of the rope (the solid red arrow marked 0) crosses the magnetic null point (the green slanted cross). The red dashed arrows marked 1 and 2 limit the cross section of the expanding rope. A selected magnetic field line (thick blue) denotes a magnetic loop of the West dipole, which was the major partner of the eruptive rope in the creation of the spheromak.

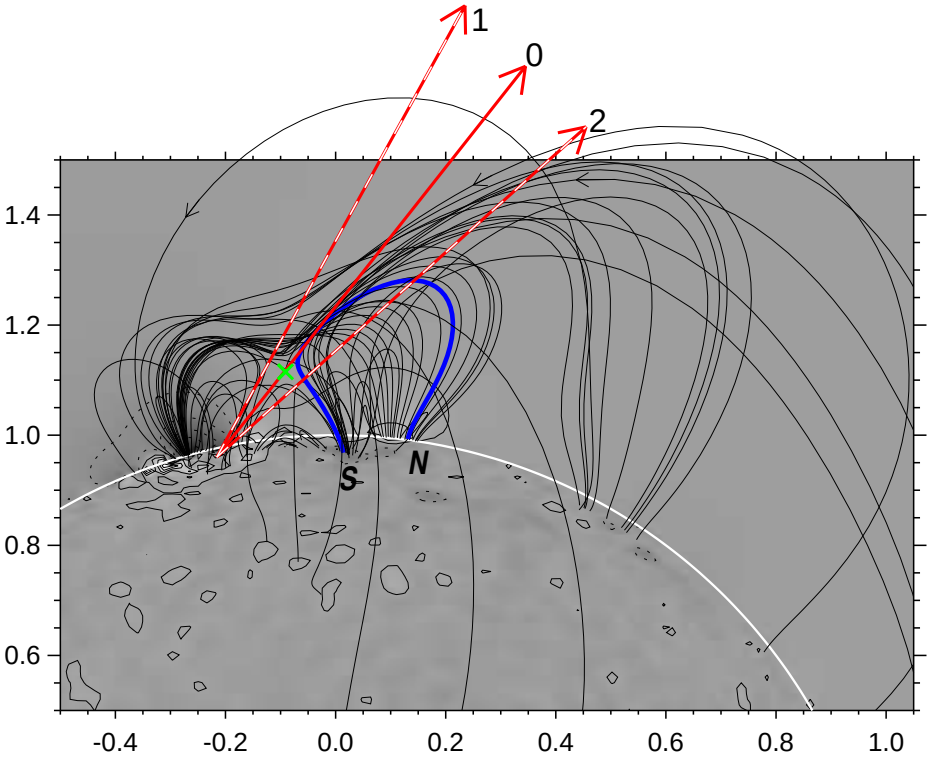

Figure 12. Side view of the magnetic configuration including arrows that indicate the trajectory of the upper part of the magnetic flux rope replacing the erupting filament F1. The trajectory of the rope (0) crosses a magnetic null point (green slanted cross). The cross section of the expanding rope is limited with the red dashed arrows 1 and 2. The thick solid curves correspond to the magnetic field lines. The blue magnetic field line denotes the magnetic flux from the West dipole (same as in Figure 8b). The thin contours on the solar surface correspond to the magnetic field values in steps of 34 G; they are −25 G (dotted) and +9 G (continuous) away from the stronger-field regions near the limb. The thick white circle denotes the solar limb. The axes are in solar radii from the solar disk center.

The interaction between the eruptive magnetic flux rope and surrounding magnetic fields can result in two effects. One is the redistribution of masses due to magnetic reconnection between the flux rope and the outer magnetic domain. This domain contains field lines, which reach the solar surface far from the quadrupole. In the projection presented in Figure 12, the red solid line 0 is tangent to such field lines. This effect is represented in Figure 13 as implied in two-dimensional reconnection models. Another effect is a kinematic linkage between the interacting structures. This essentially three-dimensional effect is used in a scheme presented in Figure 14.

Figure 13 shows a cross section of the top of the magnetic flux rope. This section moves along the external magnetic field B with a velocity V. In Figure 12 this situation corresponds to the position of the flux rope's center just after passing the magnetic null. The two circles to the left of the figure are poloidal field lines of the flux rope. Cool plasma enclosed between them is denoted by the

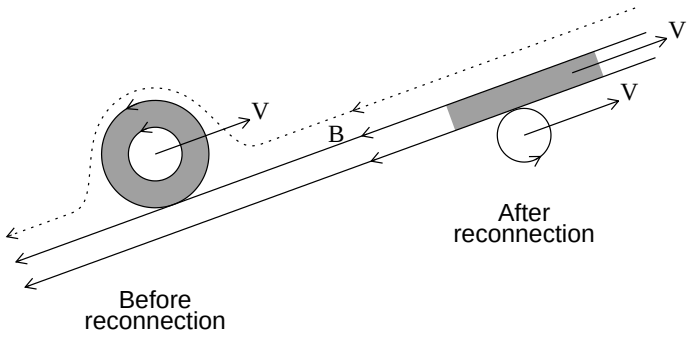

Figure 13. Mass depletion in the eruptive filament moving along the magnetic field. Left: two circular poloidal field lines indicate the cross section of the flux rope representing the erupting filament. Cool plasma between them (gray shading) moves together with the rope with a velocity V. Right: after magnetic reconnection. The center of the rope displaces across the outer field **B**, and cool plasma continues moving along **B**.

gray shading. The situation after magnetic reconnection is shown to the right of the figure. The center of the flux rope has shifted across B, while plasma (gray) has departed from the flux rope and moves along the outer field B. The scheme in Figure 13 is basically similar to Figure 6 in Grechnev *et al.* (2013). The apparent difference between the schemes is due to different directions of motions of the eruptive filaments through the magnetic null point in the quadrupolar magnetic configuration.

The 2D scheme in Figure 13 does not change if we introduce an additional homogeneous magnetic field, $B_\perp$, perpendicular to the plane of the figure without fixed ends and consider a non-compressive plasma. During magnetic reconnection, the frozen-in $B_\perp$ components of the total magnetic field are mixed like pens in a box without any effect on the process presented. However, this is not the case. The magnetic field perpendicular to the plane of the figure is strongly inhomogeneous being concentrated in the curved toroidal flux rope, which continues its motion governed almost entirely by the toroidal propelling force. Reconnection creates new three-dimensional field lines between the footpoints of the eruptive flux rope and those of the outer field lines involved in the reconnection process. The outcome is as follows: i) the eruptive filament loses mass, ii) the propelling toroidal force decreases faster than without reconnection, iii) the disintegrating eruptive flux rope separates from cool plasma spreading out behind it.

5.3. Formation of the Right-Handed Spheromak

We have found that the compact magnetic cloud in the 18–20 November 2003 event could be the result of the redistribution of the magnetic helicity after the interaction between the left-handed eruptive filament and the West dipole D_W. The conclusion about the positive mutual helicity between the pre-eruptive filament F1 and the West dipole drawn in Section 4 implies the inequality $h_\mathrm{F1} < h_\mathrm{W}$. This means that the height above the photosphere, h_F1, of the red loop, which

represents filament F1 in Figure 8, was less than that of the blue loop, which represents the loops belonging to dipole $D_{\rm W}$. This was really the case before the eruption. If the inequality would have been the reverse; then, the sign of the mutual helicity would have changed. In an intermediate case, $h_{\rm F1} = h_{\rm W}$, the mutual helicity is zero. The conservation of the total magnetic helicity restricts the choice of possible options for the subsequent dynamic reconfiguration of eruptive magnetic structures. In the absence of a clear idea about the formation mechanism of a compact right-handed spheromak-like configuration (called henceforth the spheromak for brevity), we use the following heuristic consideration.

Let us consider a straight trajectory along which the centroid of the eruptive filament moves. Arrow 0 in Figure 12 corresponds to this trajectory across the magnetic null point. The passage of the centroid through the null point (whose position is assumed to be fixed) corresponds to the equality $h_{\rm F} = h_{\rm W}$, where $h_{\rm F}$ is the height of the centroid. This equality means that the mutual helicity between the moving filament and the loops anchored to the West dipole, $H_{\rm m}^{\rm mut}$(F, W), becomes zero. To keep $H_{\rm m}^{\rm mut}$(F, W) > 0 until the onset of the interaction between these structures, the trajectory of the eruptive filament should be below the null point. This could correspond to, *e.g.*, arrow 2 in Figure 12, if the condition $h_{\rm F1} < h_{\rm W}$, which was valid before the eruption, is also valid in the dynamic regime. In this case, the clockwise angle between arrows 0 and 2 corresponds to a positive mutual helicity. Similarly, arrow 1 in Figure 12 corresponds to a trajectory above the null point. Some consequences of this geometry including magnetic reconnection and mass depletion are shown in the two-dimensional Figure 13. The counter-clockwise angle between arrows 0 and 1 corresponds to a negative mutual helicity between the eruptive filament and the loops of the West dipole.

Figure 14 presents a hypothetical 3D scheme for the formation of a right-handed spheromak, if the trajectory is below the null point. The relative position of the red and blue thick solid loops in Figure 14a is the same as in Figure 8b, which shows the situation before the eruption (t_0). The active red loop represents the left-handed eruptive filament during subsequent times $t_1, ..., t_5$. The passive blue loop is anchored to the West dipole involved in the eruption. The red and blue dotted lines represent the modified shapes of the red and blue loops just after the onset of the interaction. The expanding red loop embraces the leg of the blue loop rooted in Rb and takes a Y-like shape (*cf.* Figure 1). The stretching of the red and blue magnetic structures in Figure 14b leads to the formation of secondary loops which are linked. Magnetic reconnection results in the detachment in Figure 14c of the secondary magnetic loops from their parent loops. A closed system of the orthogonal red and blue magnetic rings is formed. The blue ring developed from the magnetic flux of the West dipole. We neglect its self-helicity and represent it as a system of non-twisted thin blue rings instead of a single thick blue ring. The magnetic pressure separates these rings (not interconnected) from each other, and they get distributed along the red ring. Remnants of its negative helicity annihilate in this way (Figure 14d). A right-handed spheromak is formed. The direction of its motion does not necessarily coincide with the direction, in which the eruptive filament, which takes back its shape, moves (the thick red arrow).

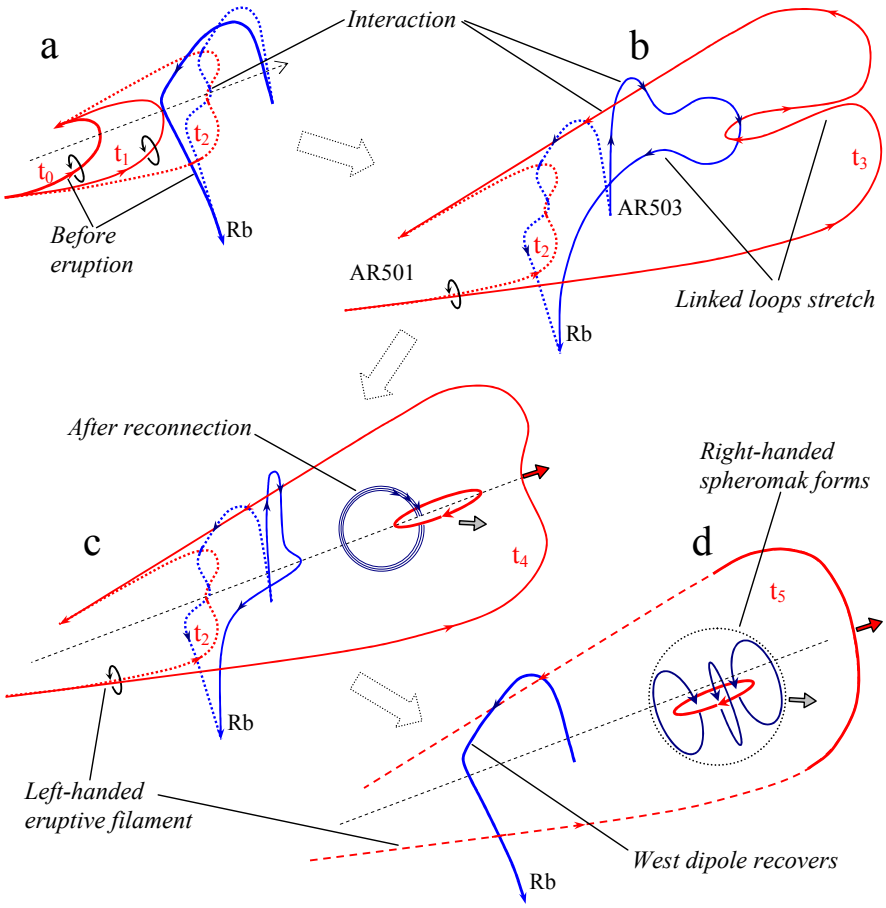

Figure 14. A hypothetical development of the situation presented in Figures 8b and 10 for the case when the trajectory (black dashed line) of the eruptive filament (active red loop) passes below the magnetic null point (arrow 2 in Figure 12). The blue loop is anchored to the West dipole involved in the eruption. Rb is the bifurcation region shown in Figures 1, 8, and 11. (a) t_0: denotes the time before the eruption; the interaction of the loops starts at t_1. The dotted lines at t_2 show the loops just after the onset of their interaction. The expanding red loop embraces the leg of the blue loop rooted in Rb and takes the Y-like shape (*cf.* Figure 1). (b) The stretching of the red and blue magnetic structures results in the formation of secondary loops which are linked. (c) Magnetic reconnection detaches the secondary loops from the parent ones. A closed system of red and blue magnetic rings is formed. (d) The blue rings separate from each other and distribute along the red ring thus destroying remnants of its left helicity. A right-handed spheromak develops. The apparent intersections of the blue and red loops in panels (a)–(d) are due to the projection effect and do not imply the possibility of reconnection. Figure 4 roughly outlines the dynamic reconfiguration presented in panels (a) and (b) of this figure, but viewed from a different angle.

5.4. Observational Consequences of the Proposed Schemes

The outcome of the process presented in Figure 14 is the formation of two different eruptive structures sharing their positive and negative magnetic helicity. The first structure is a modification of the parent left-handed eruptive filament F1, which recovers after the bifurcation and moves in the southwestern sector of the solar disk (Figure 1). The second structure is the right-handed spheromak, which was created due to the catastrophe of the filament observed as its bifurcation.

Formally assuming that the effects presented in Figures 13 and 14 coexisted in the real eruptive process, we come to the following conclusion. The bifurcation of the eruptive filament F1 was accompanied by the decrease of its poloidal flux and mass depletion. The loss of mass accounts for the absence of a conspicuous core in CME2, which appeared in LASCO images in the same southwestern sector, where the eruptive filament F1 moved. The Y-like trace of the mass, which has not left the Sun, carries information about the deformation of the magnetic flux rope in the vicinity of the magnetic null point. If the magnetic cloud, which reached Earth, would have been associated with CME2, then its magnetic helicity should be negative rather than positive. This association seemed to be plausible in the first studies of the 18–20 November 2003 event, but was ruled out in our Paper II.

In our considerations, we called the 'spheromak' a spheromak-like force-free magnetic configuration. The development of a such a configuration should be accompanied by a transformation of the magnetic energy excess of the interacting pre-spheromak structures into the kinetic energy of chaotic or directed plasma motions. It is possible that some part of this kinetic energy had gone into the formation of a wave, possibly a shock, propagating away from the formation site of the spheromak. An indication of such a wave is presented in Paper II (see also Section 4.1, last paragraph).

While constructing the scheme in Figure 14, we pursued to have as a result the compact size and positive helicity of the developing magnetic structure to match the MC, which actually hit Earth. The spheromak meets these requirements. However, our hypothetical scheme does not guarantee an earthward direction of the spheromak. There are additional indications supporting that the spheromak has actually reached Earth.

The formation of the spheromak in Figure 14 is due to the interaction of different-temperature plasma structures, *i.e.*, the cool eruptive filament and the magnetic flux of the West dipole frozen into the coronal plasma. Probably, this circumstance determined the atypically high inhomogeneity of the temperature distribution in the 20 November MC mentioned in Section 1.

The axial magnetic field of the spheromak in Figure 14 is formed from the magnetic flux of the West dipole. Therefore, the orientation of the axial field of the spheromak should be close to the direction of the vector $\mathbf{D}_{\mathrm{W}}$ in Figure 10. In turn, the inclination of $\mathbf{D}_{\mathrm{W}}$ to the ecliptic plane is reasonably close to the inclination of the MC (Section 4.3, last paragraph).

To conclude this section, we note that the scheme of the interaction between the red and blue loops in the case of an upper trajectory 1 in Figure 12 also provides the possibility to form a spheromak, but with a negative helicity. Most

likely, this option did not occur in this event, as supported by the downward displacement of the central part of the eruptive flux rope in Figure 13. In the magnetic configuration presented in Figure 12 this effect works in the same direction both before the passage of the null point by arrow 0 and after it. Thus, the lower trajectory appears to be preferential and the only possibly one in this particular event.

6. Summary

The scenario of the 18 November 2003 event does not correspond to the concept of a simple eruption directly from AR 501, in which the twist helicity of an eruptive structure or active region determines the handedness of the interplanetary magnetic cloud. The NLFF extrapolation of AR 501 shows an excess of negative twist, which is opposite to the positive sign of twist in the MC. To solve this contradiction, we have used the positive mutual helicity between the pre-eruptive filament and the flux tubes of a magnetic domain of the large-scale quadrupole configuration. The interaction of these magnetic fluxes presumably occurred as the eruptive filament passed in the neighborhood of the coronal magnetic null point. The positive mutual helicity of these two fluxes changed through magnetic reconnections into the positive self-helicity of a spheromak-like structure, whose geometry and parameters correspond to the magnetic cloud, which reached Earth. In Paper IV, we analyze the interplanetary disturbance responsible for the 20 November superstorm and outline the overall scenario of the whole event.

Acknowledgements We thank V. Yurchyshyn, who kindly supplied the vector magnetogram of AR 501 observed at BBSO, and M. Temmer for the Hα data. We thank the co-authors of our Papers I, II, and IV, who are not involved in this study. We appreciate an anonymous reviewer for valuable remarks and comments. We are grateful to the instrumental teams of the Kanzelhöhe Solar Observatory; TRACE and CORONAS-F missions; MDI and EIT on SOHO (ESA and NASA) for the data used here. This study was supported by the Russian Foundation of Basic Research under grants 11-02-00757, 11-02-01079, 12-02-00008, 12-02-92692, and 12-02-00037, and the Ministry of Education and Science of Russian Federation, projects 8407 and 14.518.11.7047.

References

Afanasyev, A.N., Uralov, A.M.: 2012, *Solar Phys.* **280**, 561.

Attrill, G.D.R., Harra, L.K., van Driel-Gesztelyi, L., Démoulin, P.: 2007, *Astrophys. J. Lett.* **656**, L101.

Berger, M.A.: 1998, In: Webb, D.F., Schmieder, B., Rust, D.M. (eds.) *IAU Colloq. 167: New Perspectives on Solar Prominences.* San Francisco, CA. ASP Conf. Ser. **150**, 102.

Chandra R., Pariat, E., Schmieder, B., Mandrini, C.H., Uddin, W.: 2010, *Solar Phys.* **261**, 127.

Delaboudinière, J.-P., Artzner, G.E., Brunaud, J., Gabriel, A.H., Hochedez, J.F., Millier, F., Song, X.Y., Au, B., *et al.*: 1995, *Solar Phys.* **162**, 291.

Démoulin, P., Pariat, E., Berger, M.A.: 2006, *Solar Phys.* **233**, 3.

Gopalswamy, N., Yashiro, S., Michalek, G., Xie, H., Lepping, R.P., Howard, R.A.: 2005, *Geophys. Res. Lett.* **32**, L12S09.
Grechnev, V.V., Kuzmenko, I.V., Chertok, I.M., Uralov, A.M.: 2011a, *Astron. Rep.* **55**, 637.
Grechnev, V., Kuzmenko, I., Uralov, A., Chertok, I., Kochanov, A.: 2013, *Publ. Astron. Soc. Japan 65*, SP1, S10.
Grechnev, V.V., Uralov, A.M., Chertok, I.M., Belov, V.A., Filippov, B.P., Slemzin, V.A., Jackson, B.V.: 2014a, *Solar Phys.* submitted.
Grechnev, V.V., Uralov, A.M., Chertok, I.M., Kuzmenko, I.V., Afanasyev, A.N., Meshalkina, N.S., Kalashnikov, S.S., Kubo, Y.: 2011b, *Solar Phys.* **273**, 433.
Grechnev, V.V., Uralov, A.M., Chertok, I.M., Slemzin, V.A., Filippov, B.P., Egorov, Ya.I., Fainshtein, V.G., Afanasyev, A.N., Prestage, N., Temmer, M.: 2014b, *Solar Phys. 289*, 1279.
Grechnev, V.V., Uralov, A.M., Slemzin, V.A., Chertok, I.M., Filippov, B.P., Rudenko, G.V., Temmer, M.: 2014c, *Solar Phys. 289*, 289.
Grechnev, V.V., Uralov, A.M., Slemzin, V.A., Chertok, I.M., Kuzmenko, I.V., Shibasaki, K.: 2008, *Solar Phys.* **253**, 263.
Handy, B.N., Acton, L.W., Kankelborg, C.C., Wolfson, C.J., Akin, D.J., Bruner, M.E., Caravalho, R., Catura, R.C., *et al.*: 1999, *Solar Phys.* **187**, 229.
Harra, L.K., Sterling, A.C.: 2001, *Astrophys. J. Lett.* **561**, L215.
Imada, S., Hara, H., Watanabe, T., Kamio, S., Asai, A., Matsuzaki, K., Harra, L.K., Mariska, J.T.: 2007, *Publ. Astron. Soc. Japan* **59**, 793.
Jin, M., Ding, M.D., Chen, P.F., Fang, C., Imada, S.: 2009, *Astrophys. J.* **702**, 27.
Leamon, R.J., Canfield, R.C., Jones, S.L., Lambkin, K., Lundberg, B.J., Pevtsov, A.A.: 2004, *J. Geophys. Res.A* **109**, 5106.
Lin, R.P., Dennis, B.R., Hurford, G.J., Smith, D.M., Zehnder, A., Harvey, P.R., *et al.*: 2002, *Solar Phys.* **210**, 3.
Lugaz, N., Downs, C., Shibata, K., Roussev, I.I., Asai, A., Gombosi, T.I.: 2011, *Astrophys. J.* **738**, 127.
Lui, A.T.Y.: 2011, *Space Sci. Rev.* **158**, 43.
Masson, S., Antiochos, S.K., DeVore, C.R.: 2013, *Astrophys. J.* **771**, 82.
McLaughlin, J.A., Hood, A.W., de Moortel, I.: 2011, *Space Sci. Rev.* **158**, 205.
Meshalkina, N. S., Uralov, A. M., Grechnev, V. V., Altyntsev, A. T., Kashapova, L. K.: 2009, *Publ. Astron. Soc. Japan* **61**, 791.
Möstl, C., Miklenic, C., Farrugia, C.J., Temmer, M., Veronig, A., Galvin, A.B., Vršnak, B., Biernat, H.K.: 2008, *Ann. Geophys.* **26**, 3139.
Oraevsky, V.N., Sobelman, I.I.: 2002, *Astron. Lett.* **28**, 401.
Oraevsky, V.N., Sobelman, I.I., Zitnik, I.A., Kuznetsov, V.D., Stepanov, A.I., Polishuk, G.M., *et al.*: 2003, *Adv. Space Res.* **32**, 2567.
Parnell, C.E., Smith, J.M., Neukirch, T., Priest, E.R.: 1996, *Phys. Plasmas* **3**, 759.
Rudenko, G.V.: 2001, *Solar Phys.* **198**, 5.
Rudenko, G.V., Grechnev, V.V.: 1999, *Astronomical Data Analysis Software and Systems VIII*, ASP Conf. Ser. **172**, 421.
Rudenko, G.V., Myshyakov, I.I.: 2009, *Solar Phys.* **257**, 287.
Scherrer, P.H., Bogart, R.S., Bush, R.I., Hoeksema, J.T., Kosovichev, A.G., Schou, J., *et al.*: 1995, *Solar Phys.* **162**, 129.
Slemzin, V.A., Kuzin, S.V., Zhitnik, I.A., Delaboudiniere, J.-P., Auchere, F., Zhukov, A.N., van der Linden, R., Bugaenko, O.I., Ignat'ev, A.P., Mitrofanov, A.V., Pertsov, A.A., Oparin, S.N., Stepanov, A.I., Afanas'ev, A.N.: 2005, *Solar Sys. Res.* **39**, 489.
Srivastava, N., Mathew, S.K., Louis, R.E., Wiegelmann, T.: 2009, *J. Geophys. Res.* **114**, A03107.
Yurchyshyn, V., Hu, Q., Abramenko, V.: 2005, *Space Weather*, **3**, S08C02.
Zhang, M., B. C. Low: 2003, *Astrophys. J.* **584**, 479.
Zhitnik, I.A., Bougaenko, O.I., Delaboudinière, J.-P., Ignatiev, A.P., Korneev, V.V., Krutov, V.V., Kuzin, S.V., Lisin, D.V., *et al.*: 2002, *Proc. 10th European Solar Physics Meeting, Prague (ESA SP-506)*, 915.
Zuccarello, F.P., Bemporad, A., Jacobs, C., Mierla, M., Poedts, S., Zuccarello, F.: 2012, *Astrophys. J.* **744**, 66.